How to cite: *Angew. Chem. Int. Ed.* **2025**, *64*, e202418269
doi.org/10.1002/anie.202418269

Metalated Graphynes

A Highly Conjugated Nickel(II)-Acetylide Framework for Efficient Photocatalytic Carbon Dioxide Reduction

Yingying Qin, Yang Wang, Jian Lu, Linli Xu, and Wai-Yeung Wong**

Abstract: The incorporation of transition-metal single atoms as molecular functional entities into the skeleton of graphdiyne (GDY) to construct novel two-dimensional (2D) metal-acetylide frameworks, known as metalated graphynes (MGYs), is a promising strategy for developing efficient catalysts, which can combine the tunable charge transfer of GDY frameworks, the catalytic activity of metal and the precise distribution of single metallic centers. Herein, four highly conjugated MGY photocatalysts based on Ni^{II}, Pd^{II}, Pt^{II}, and Hg^{II} were synthesized for the first time using the 'bottom-up' strategy through the use of M–C bonds (–C≡C–M–C≡C–). Remarkably, the Ni^{II}-based graphyne (TEPY-Ni-GY) exhibited the highest CO generation rate of 18.3 mmol g^{-1} h^{-1} and a selectivity of 98.8 %. This superior performance is attributed to the synergistic effects of pyrenyl and –C≡C–Ni(PBu_3)$_2$–C≡C– moieties. The pyrenyl block functions as an intramolecular π-conjugation channel, facilitating kinetically favorable electron transfer, while the –C≡C–Ni(PBu_3)$_2$–C≡C– moiety serves as the catalytic site that enhances CO_2 adsorption and activation, thereby suppressing competitive hydrogen evolution. This study provides a new perspective on MGY-based photocatalysts for developing highly active and low-cost catalysts for CO_2 reduction.

Introduction

Graphdiyne (GDY), an emerging 2D carbon allotrope, is composed of *sp*- and sp^2-hybridized carbon atoms with benzene rings connected by acetylene linkages.[1–5] The distinct structural advantages of GDY endow it with controllable electronic properties and superior electron transfer capability.[6–10] Compared to conventional sp^2-hybridized carbon allotropes such as fullerene, carbon nanotubes, and graphene, the unique alkyne-rich structure of GDY makes it an ideal platform for anchoring zero/low-valent metal atoms and flexibly adjusting the coordination environment.

To date, a variety of GDY-derived metal atomic catalysts based on Fe,[11] Ni,[12] Cu,[13,14] Pd,[15] Pt,[16] and Au,[17] among others, have been developed, exhibiting decent physicochemical properties. In these reported catalysts, the metal atoms are only anchored on the surface or within the cavities of GDY through organometallic σ/π-coordination,[18,19] resulting in inhomogeneous structures and unstable active sites. This makes it challenging to understand the catalytic mechanisms at the molecular or atomic level. To address these issues, metal single-atoms were precisely introduced into the GDY skeleton as another molecular functionality via metal-bis(acetylide) bonds (–C≡C–M–C≡C–), creating a novel class of 2D metal-acetylide framework known as metalated graphyne (MGY). In recent years, GDY structures incorporating metal ions such as Ag^I,[20] Au^I,[21] and Hg^{II}[22] have been realized. The overlap between the *d* orbitals of metal and the *p* orbitals of the alkynyl units stabilizes the single metal atoms and redistributes the electron density within the MGY frameworks, making them potentially good molecular catalysts.[23,24] However, MGY-based molecular catalysts are still in their infancy stages. More types of MGY need to be designed and developed by varying the types of metal ions and multi-acetylenic ligands, with a particular focus on using low-cost and highly catalytically active metal centers.

Recent research in molecular catalysts has focused on designing efficient electron transport channels from ligands to the metal active center to ensure that more electrons participate in the CO_2 reduction reaction (CO_2RR). Efficient electron transfer can increase the charge density of the metal *d* orbital, allowing it to combine with the π* orbital of CO_2. This facilitates the C adsorption mode between CO_2 and the catalytic sites, leading to CO generation while inhibiting the competing hydrogen evolution reaction.[25,26] According to the previous reports, increasing the degree of intramolecular conjugation to delocalize free electrons is the most effective way to achieve this goal. For example, Ye et al. demonstrated that the N-CP-A conjugated polymer consisting of pyrenyl units and alkynyl groups, exhibited a

[*] Dr. Y. Qin, Dr. Y. Wang, Dr. L. Xu, Prof. W.-Y. Wong
Department of Applied Biology and Chemical Technology and Research Institute for Smart Energy
The Hong Kong Polytechnic University
Hung Hom, Hong Kong, P. R. China
E-mail: wai-yeung.wong@polyu.edu.hk
linli.xu@polyu.edu.hk

Dr. J. Lu
School of Fashion and Textiles
The Hong Kong Polytechnic University
Hung Hom, Hong Kong, P. R. China

higher charge carrier mobility of 0.35 $cm^2 V^{-1} s^{-1}$, compared to N-CP-D without the alkynyl group (0.25 $cm^2 V^{-1} s^{-1}$), resulting in a higher CO_2 conversion efficiency.[27] Cao and co-workers synthesized a pyrazolyl-based Ni-MOF with a highly π-conjugated system that enhanced the transfer efficiency of ligand-to-node electrons, leading to higher CO and CH_4 production rates.[28] Therefore, rational construction of highly π-conjugated moieties in MGY, along with the synergistic optimization of the intermediate reaction potential barriers and electron transfer using the –C≡C–M–C≡C– blocks, can ensure high activity and selectivity towards CO_2RR catalysis.

Based on the aforementioned considerations, we report four novel MGY catalysts (named TEPY-M-GYs) with excellent charge transport characteristics, which are assembled using the connecting nodes of four transition-metal groups (M = $Ni^{II}(PBu_3)_2$, $Pd^{II}(PBu_3)_2$, $Pt^{II}(PBu_3)_2$, and Hg^{II}) and the highly π-conjugated organic ligand 1,3,6,8-tetraethynylpyrene (TEPY). The pyrene group in our design possesses extensive π-conjugation, which effectively enhances the photo-generated charge dynamics to the M^{II}-bis(acetylide) moieties, providing sufficient electrons for the CO_2RR. Among the four MGYs, TEPY-Ni-GY exhibited the highest activity and selectivity for photocatalytic CO_2RR. The –C≡C–$Ni(PBu_3)_2$–C≡C– blocks serve as the most active catalytic sites, optimizing CO_2 adsorption and activation energy, and stabilizing key intermediates to enhance CO_2 conversion efficiency and product selectivity. These TEPY-M-GYs offer a unique opportunity to investigate the mechanism of catalytic active sites at the atomic level and open up new possibilities for exploring low-cost and highly active GDY-based catalytic materials.

Results and Discussion

In our previous works, mercurated graphynes have been reported as efficient 2D photo-functional materials and catalysts.[24] Here, four transition metal ions (Ni^{II}, Pd^{II}, Pt^{II} and Hg^{II}) were successfully introduced into GDY framework through base-catalyzed dehydrohalogenation reactions. These reactions involved *trans*-$Ni(PBu_3)_2Cl_2$, *trans*-$Pd(PBu_3)_2Cl_2$, *trans*-$Pt(PBu_3)_2Cl_2$ or $HgCl_2$ and the highly conjugated ligand TEPY, resulting in the formation of TEPY-M-GYs (M = $Ni^{II}(PBu_3)_2$, $Pd^{II}(PBu_3)_2$, $Pt^{II}(PBu_3)_2$, and Hg^{II}). While TEPY-Hg-GY was synthesized in a solvent mixture of methanol (MeOH) and tetrahydrofuran (THF) with triethylamine (TEA) as the base catalyst only the other TEPY-M-GYs were synthesized in THF as the solvent, with both CuI and TEA as the catalysts. The transition-metal centers (Ni^{II}, Pd^{II}, Pt^{II}, and Hg^{II}) were incorporated into the GDY framework through metal-bis(acetylide) linkages (–C≡C–M–C≡C–) (Scheme 1).

The powder X-ray diffraction (PXRD) experiment was conducted to elaborate the crystalline nature of these TEPY-M-GYs. As shown in Figure S1, the experimental PXRD pattern of TEPY-Ni-GY exhibited two broad diffraction peaks (black curve): one in the low-angle region at approximately 2θ = 9.1° corresponding to the (110) plane,

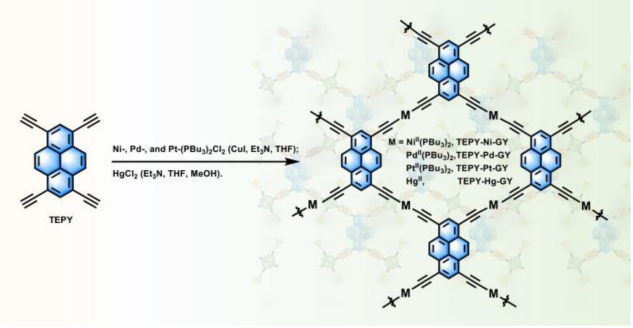

Scheme 1. Illustration of the synthesis of TEPY-M-GYs (M = $Ni^{II}(PBu_3)_2$, $Pd^{II}(PBu_3)_2$, $Pt^{II}(PBu_3)_2$, and Hg^{II}).

and another peak at approximately 2θ = 20.4°corresponding to the (001) plane, indicating the formation of a 2D layered material via π–π stacking in the *c* direction. Notably, no diffraction peaks corresponding to nickel salts or nickel nanoparticles were observed, suggesting that the Ni^{II}-complexes existed in the form of a coordination structure within the 2D framework of GDY. Materials Studio was used to simulate and optimize the structural models of TEPY-M-GYs. The TEPY-Ni-GY conformed to a structure with an aligned AA stacking mode, and the optimized unit cell parameters were a = 18.21 Å, b = 15.18 Å, c = 3.71 Å, α = 90.85°, β = 88.74°, and γ = 127.05°. Similarly, the experimental PXRD patterns of TEPY-Pd-GY, TEPY-Pt-GY, and TEPY-Hg-GY also matched well with the calculated results from the aligned AA stacking mode (Figures S2–S4), demonstrating that the introduction of different metal ions had a negligible effect on their structural packing mode.

Fourier-transform infrared (FT-IR) spectra confirmed the success of the dehydrohalogenation reaction between the TEPY monomer and metal complexes (Figure 1a). The complete disappearance of the –C≡CH stretching vibration peak at 3280 cm^{-1} for TEPY (Figure S5), along with the appearance of a new characteristic peak corresponding to the –C≡C– stretching vibration band at 2140 cm^{-1} in TEPY-M-GYs, verified the successful formation of the –C≡C–M–C≡C– unit in the framework. Additionally, the C–H stretching vibration peak of *n*-Bu was observed (3200–3500 cm^{-1}) in TEPY-Ni-GY, TEPY-Pd-GY, and TEPY-Pt-GY, further indicating the successful formation of metal-acetylide networks.[22–23] The chemical structure of TEPY-Ni-GY was further confirmed by the solid-state ^{13}C NMR spectrum (Figure 1b). The peaks at 12.7 and 23.5 ppm belonged to the signal of *n*-Bu and the peaks at around 80.6 and 95.3 ppm could be attributed to the carbon atoms of the acetylene linkage (–C≡C–), while the broad peak in the range of 100–150 ppm was assigned to the sp^2-bonded carbon in the backbone.[29] The N_2 sorption isotherm measurements disclosed the typical type-II isotherm for all TEPY-M-GYs, revealing their microporous structural features (Figure 1c). The corresponding Brunauer–Emmett–Teller (BET) specific surface areas of TEPY-Ni-GY, TEPY-Pd-GY, TEPY-Pt-GY, and TEPY-Hg-GY were calculated

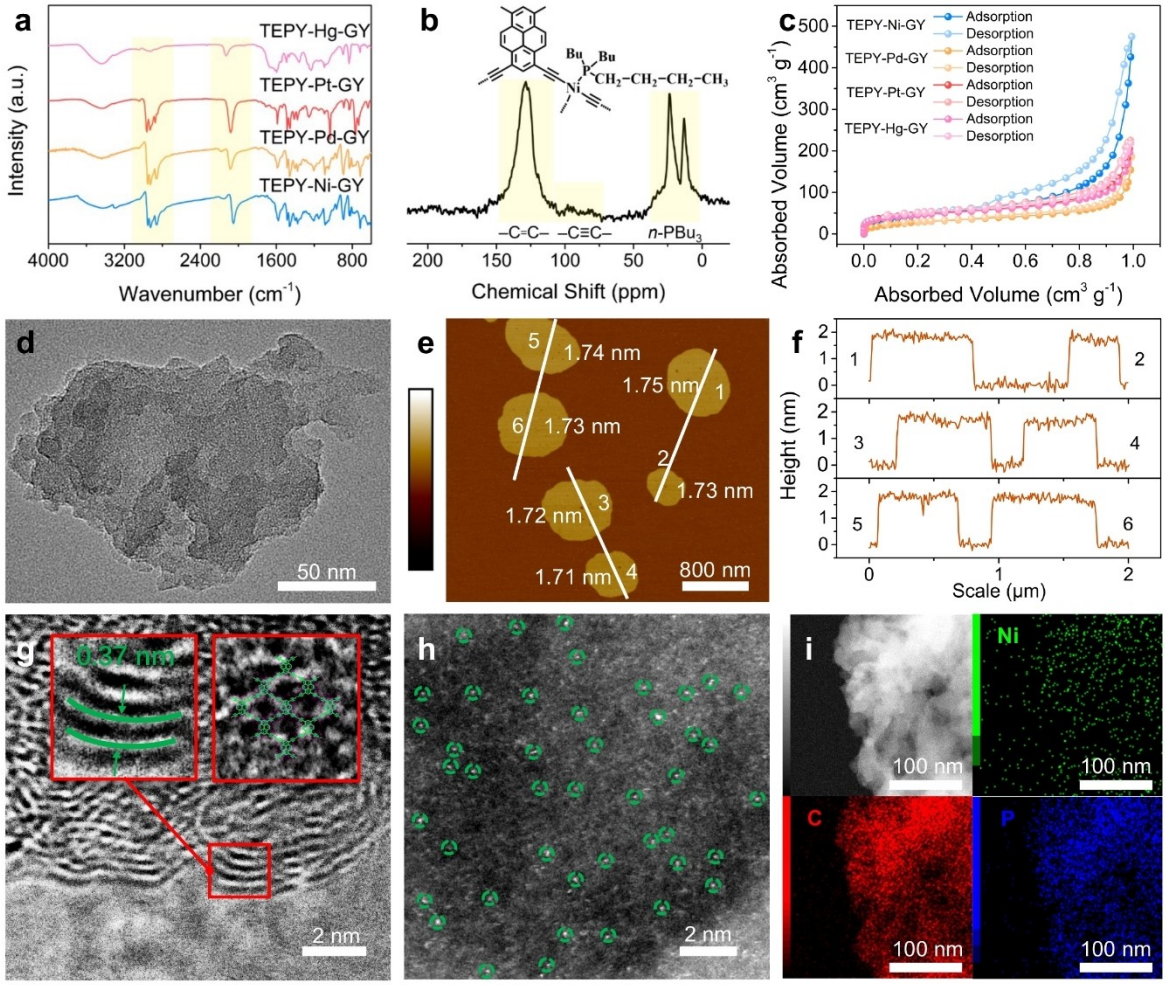

Figure 1. (a) FT-IR spectra of TEPY-M-GYs. (b) Solid-state ^{13}C NMR spectrum of TEPY-Ni-GY. The assignments of ^{13}C chemical shifts for TEPY-Ni-GY are indicated in its chemical structure. (c) N_2 sorption isotherms of TEPY-M-GYs at 77 K. (d) TEM image, (e) AFM image, and (f) the corresponding height profiles along the marked white line of TEPY-Ni-GY nanosheets. (g) HRTEM image (inset: magnified portion) and (h) aberration-corrected HAADF-STEM image of TEPY-Ni-GY (Ni centers are marked with green circles). (i) HAADF-STEM and the corresponding EDX mapping images of TEPY-Ni-GY. EDX mapping of Ni, P and C elements are shown with green, blue, and red colors, respectively.

to be 170.6, 106.9, 167.0 and 162.9 $m^2 g^{-1}$, respectively. The pore size distributions confirmed that the real pore sizes of these TEPY-M-GYs were centered at 1.31–1.33 nm (Figure S6), which were close to the theoretical values in the AA stacking model.

The morphologies of TEPY-M-GYs were characterized by scanning electron microscopy (SEM) and transmission electron microscopy (TEM) (Figures S7–S13). TEPY-Ni-GY exhibited an 2D lamellar morphology (Figure 1d). The few-layer nanosheets of TEPY-Ni-GY on the silicon wafer presented a planar film with a thickness of approximately 1.7 nm, consisting of four or five monolayers (Figure 1e–f). The high-resolution TEM (HRTEM) image of TEPY-Ni-GY showed distinct lattice fringes with a spacing of ~3.7 Å (Figure 1g), corresponding to its (001) plane. This result was also confirmed by the PXRD of TEPY-Ni-GY, which displayed a characteristic peak at $2\theta = 24°$ with a *d*-spacing of 3.71 Å, matching well with the results obtained from the DFT calculations (Figure S1).[30] Besides, the TEM images revealed the parallelogram lattice structure in TEPY-Ni-GY, consistent with the simulation results. The aberration-corrected high-angle annular dark-field scanning transmission electron microscopy (AC-HAADF-STEM) of TEPY-Ni-GY showed many isolated bright dots marked with green circles, which were identified as atomically dispersed Ni centers (Figure 1h). Meanwhile, the SEM images and the corresponding energy dispersive X-ray (EDX) element mapping of TEPY-Ni-GY demonstrated that Ni, C, and P elements were homogeneously distributed throughout the entire TEPY-Ni-GY matrix, indicating that the continuous Ni-containing framework was successfully established (Figure 1i). The metal content in TEPY-M-GYs was determined by inductively coupled plasma mass spectrometry (ICP-MS) (Table S1), and the loading amounts of metal ions were consistent with the molecular structures of TEPY-M-GYs. The uniformly arranged structure, conductive skeleton, and enriched metallic active sites of TEPY-M-GYs would be substantially favorable for the high activity of catalysts. The

chemical structures and morphologies of these novel TEPY-M-GYs were confirmed by various experimental and theoretical methods.

Moreover, the thermal stability of TEPY-M-GYs was investigated by thermogravimetric analysis (TGA), which showed that the samples remained stable up to approximately 200 °C under a N_2 atmosphere (Figure S14). Additionally, TEPY-Ni-GY was dispersed in different solvents for 24 h, and no significant changes were observed in the position and intensity of the PXRD characteristic peaks (Figure S15). These experimental results indicate that TEPY-Ni-GYs possess excellent thermal and chemical stability, making them suitable for practical applications.

X-ray photoelectron spectroscopy (XPS) was conducted to identify the chemical composition and electronic structures of the samples (Figures S16–S19). The full survey spectrum for TEPY-Ni-GY revealed the co-existence of Ni, C, and P elements, consistent with the EDX mapping analysis. As shown in Figure 2a, the high-resolution XPS spectrum of C 1*s* was deconvoluted into seven sub-peaks, assigned to C(*sp*)–Ni (283.2 eV), C–C (sp^2, 284.2 eV), C–C (sp^3, 284.8 eV), C–C (*sp*, 285.4 eV), C–P (286.1 eV), C–O (287.0 eV), and C=O (288.1 eV).[31] The formed C(*sp*)–Ni bonds could stabilize the position of Ni ions and enhance the stability of catalyst. The presence of C–O and C=O groups was attributed to the absorbed CO_2 in the surface of samples.[19,32] The proportion of sp/sp^2 carbon is approximately 1:2, consistent with the theoretical ratio in TEPY-Ni-GY. Furthermore, in the high-resolution Ni 2*p* XPS spectrum, the two dominant characteristic peaks of Ni $2p_{1/2}$ and Ni $2p_{3/2}$ appeared at 873.6 and 856. 0 eV, along with two adjacent satellite peaks at 879.5 and 861.5 eV, suggesting the presence of positively charged $Ni^{\delta+}$ species in TEPY-Ni-GY (Figure 2b).[33] The P 2*p* XPS spectrum could be deconvoluted into two sub-peaks corresponding to P–Ni at 132.1 eV and P–C at 132.9 eV, respectively (Figure 2c).[34] X-ray absorption spectroscopy (XAS) was measured to further investigate the chemical states and coordination environments of the Ni ion in TEPY-Ni-GY, using Ni foil and NiO as reference samples. As presented in Figure 2d, the adsorption edge position of TEPY-Ni-GY closely resembles that of NiO, indicating that the Ni center has a valance state of approximately +2. The Fourier-transformed extended X-ray absorption fine structure (FT-EXAFS) spectra of the samples were displayed in Figure 2e. TEPY-Ni-GY had a main peak at around 1.64 Å, attributed to the scattering

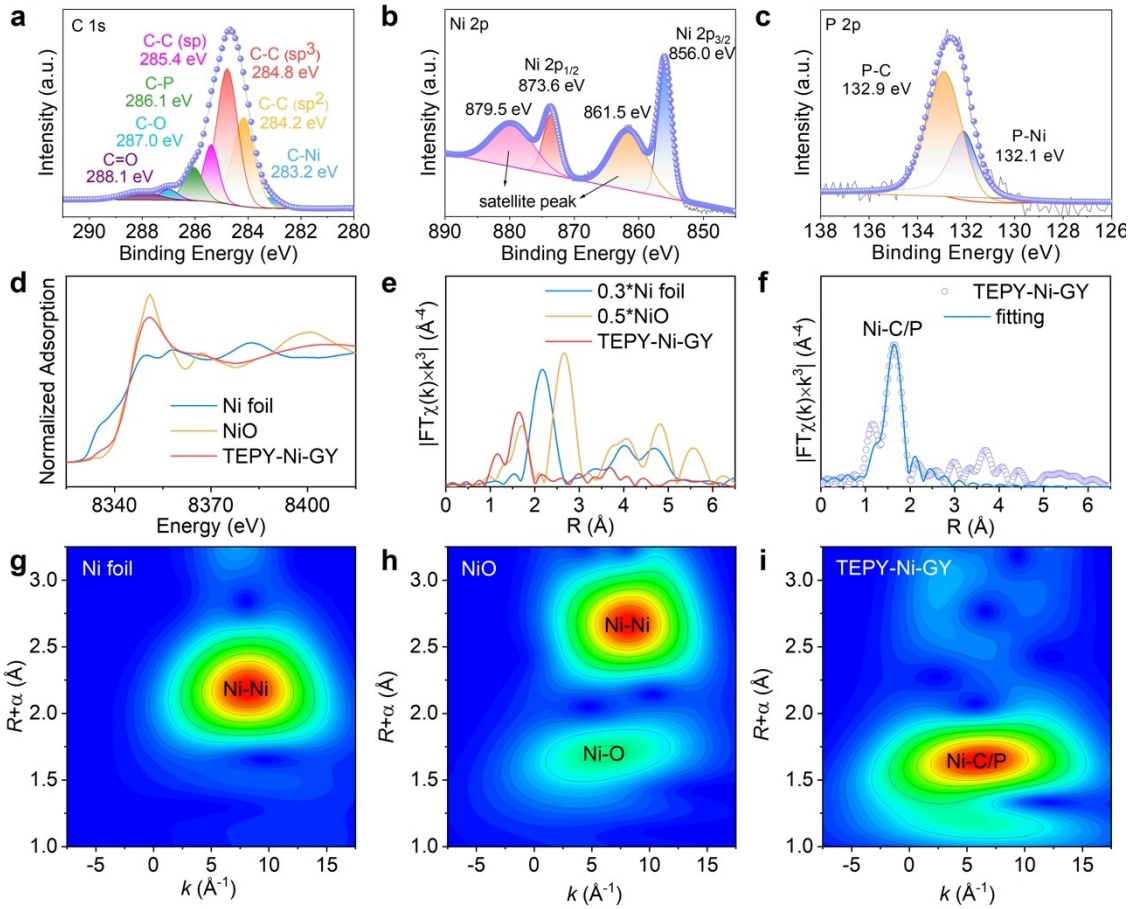

Figure 2. High-resolution XPS spectra of (a) C 1s, (b) Ni 2*p* and (c) P 2*p* for TEPY-Ni-GY. XAFS characterization of TEPY-Ni-GY, Ni foil, and NiO. (d) Ni K-edge XANES spectra and (e) the corresponding k^3-weighted FT-EXAFS spectra. Ni K-edge EXAFS (points) and curve-fit (line) for TEPY-Ni-GY shown in (f) *R*-space and in (g) *k*-space. (h–j) Wavelet transform EXAFS spectra of Ni-foil, NiO, and TEPY-Ni-GY, respectively.

interaction between Ni ions and the first coordination layer (Ni–C/P). Moreover, the Ni–Ni bond at ~2.17 Å (Ni foil) and Ni–O bond at ~1.71 Å (NiO) were not detected in the spectrum of TEPY-Ni-GY, illustrating that Ni species existed as single atoms. The fine molecular structure was verified by fitting the k^3-weighted FT-EXAFS spectra (Figures 2f, S20–S22), and the fitting analysis results of EXAFS were displayed in Table S2. The coordination number of the Ni–C/P was about 4.2, indicating that each Ni ion was bonded to two C atoms and two P atoms with an average atomic distance of approximately 2.06 Å. As shown in the wavelet transform analysis of TEPY-Ni-GY, there was only one intensity maximum at around 6.03 $Å^{-1}$ in k space (ascribed to Ni–C/P coordination), further confirming that Ni sites are atomically dispersed without aggregation in TEPY-Ni-GY (Figure 2g–i). This may be attributed to the overlap between the p orbitals of *sp*-C and the *d* orbitals of Ni^{II}, which increases the migration barrier of Ni^{II} ions, thereby effectively achieving the dispersion of single Ni centers.

According to the above exploration of the structure and features of TEPY-M-GYs, it could be proposed that the extensive π-conjugation system and catalytically active metal-bis(acetylide) sites would be instrumental for photocatalytic applications. The photocatalytic CO_2RR performance of these TEPY-M-GYs was systematically tested under AM 1.5 G simulated illumination in a CO_2-saturated atmosphere, using a mixture of acetonitrile and water (V/V = 3/1) as the solvents, triethanolamine (TEOA) as a sacrificial electron donor and $[Ru(bpy)_3]Cl_2$ as the photosensitizer. Experimental factors such as water content and catalyst quantity were optimized to enhance the photocatalytic CO_2 reduction performance (Figures S23 and S24). All TEPY-M-GYs were capable of reducing CO_2 to CO and H_2 as the primary reaction products under the above reaction conditions, while no other liquid or gaseous products were detected by ^1H nuclear magnetic resonance (^1H NMR) spectroscopy and gas chromatography-mass spectrometry (GC-MS) (Figures S25–S28). Encouragingly, TEPY-Ni-GY exhibited excellent photocatalytic CO_2RR performance over a 5 h illumination period, achieving a CO production rate of 18.3 mmol g^{-1} h^{-1}. The competitive hydrogen evolution reaction (HER) was suppressed, with a maximum output of only 231.9 μmol g^{-1} h^{-1}. Consequently, TEPY-Ni-GY demonstrated the highest selectivity of 98.8 % and activity for CO_2-to-CO conversion among the four TEPY-M-GYs (Figure 3a–b). Comparatively, the performance and selectivity of TEPY-Ni-GY for CO_2 photoreduction were superior to most reported Ni-based organic photocatalytic materials under similar reaction conditions (Table S3). To investigate the effect of branched chain length on the photocatalytic performance, three types of branched chains in the trialkylphosphine (PMe_3, PEt_3, and PBu_3) were tested. The photocatalytic performance was directly proportional to the branched chain length (Figure S29), likely due to the formation of a nano-confined space by more hydrophobic branched chains, facilitating CO_2 molecules in contact with the catalytic sites. The apparent quantum efficiency (AQE) of the photocatalytic CO_2RR over TEPY-Ni-GY was measured using different monochromatic light sources, with

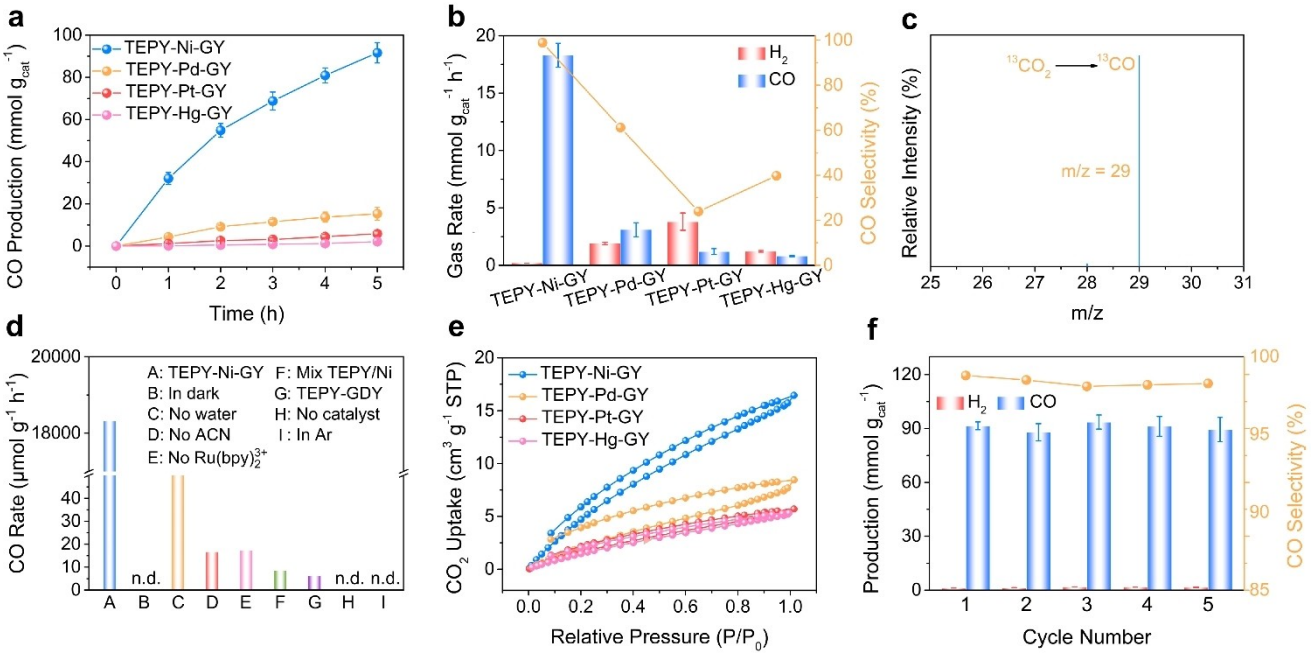

Figure 3. (a) Time-dependent production of CO under visible light irradiation (420 nm < λ < 760 nm) over a duration of 5 h using TEPY-Ni-GY (blue line), TEPY-Pd-GY (orange line), TEPY-Pt-GY (red line) and TEPY-Hg-GY (pink line) as catalysts. (b) Photocatalytic CO_2RR performance and selectivity for TEPY-> M-GYs. (c) Mass spectrum of ^{13}CO ($m/z = 29$) produced during the photocatalytic reduction of $^{13}CO_2$ over TEPY-Ni-GY. (d) Control experiments assessing the photocatalytic CO_2 reduction performance of TEPY-Ni-GY. (e) CO_2 absorption isotherms of TEPY-M-GYs at 298 K. (f) Cyclic stability tests of TEPY-Ni-GY for CO_2 photoreduction.

a maximum AQE of 1.4 % at 450 nm. The AQE values at different wavelengths followed the characteristic absorption spectrum of $[Ru(bpy)_3]Cl_2$, confirming its role as a photosensitizer in facilitating CO_2RR under visible light irradiation (Figure S30). A ^{13}C isotope tracing experiment using $^{13}CO_2$ as the photocatalytic reaction atmosphere confirmed the carbon source of the reduction products. A peak at m/z = 29 detected by GC-MS corresponded to ^{13}CO (Figure 3c), indicating that the CO product was derived from the gaseous CO_2 reactant rather than other carbon-containing species in the photocatalytic system. Control experiments demonstrated the necessity of TEPY-Ni-GY for CO_2RR, as no significant reduction products were observed in its absence, in the dark, or under an argon atmosphere, confirming the importance of the optimized catalytic conditions for CO evolution (Figure 3d).[35,36] Additionally, no carbon-based reduction products were detected under an argon atmosphere, further demonstrating that the CO product originated from CO_2 rather than the decomposition of organic substances, consistent with the ^{13}C isotope labeling experimental results. The CO_2RR activity of a physical mixture of TEPY-GDY and $Ni(PBu_3)_2Cl_2$ (denoted as mix-TEPY/Ni), as well as that of TEPY-GDY alone, was also investigated. The poor photocatalytic activity observed in both mix-TEPY/Ni and TEPY-GDY underscores the synergistic effects between the pyrenyl and –C≡C–$Ni(PBu_3)_2$–C≡C– moieties in TEPY-Ni-GY, rather than the statement that free Ni^{2+} ion or GDY acts as the catalytic active sites. The activated TEPY-Ni-GY exhibited the best CO_2 uptake ability (16.46 $cm^3 g^{-1}$) at 298 K compared to other samples, indicating that CO_2 could easily access the active sites during the photocatalytic CO_2RR process (Figures 3e and S31). The recyclability of TEPY-Ni-GY was tested through consecutive 20 h photocatalytic cycles with a recycled catalyst (Figure 3f), showing no noticeable change in CO production rate and selectivity. Structural integrity was maintained, as confirmed by XRD, FT-IR, XPS, TEM, and SEM analyses (Figures S32–S36), demonstrating the excellent stability and reusability of TEPY-Ni-GY.

The light absorption properties and electronic structures of the TEPY-M-GYs were evaluated by UV/Vis diffuse reflectance spectra (UV/Vis DRS) and Mott–Schottky (M–S) measurements. As shown in the UV/Vis DRS, TEPY-Ni-GY displayed broad and high light-harvesting capacity in the visible light and near-infrared regions compared to the other samples, demonstrating that the types of metal ions had a significant impact on the optical properties of these materials. An obvious absorption redshift was observed after the introduction of Ni^{II} ions into the GDY framework, verifying that Ni^{II} metal ions could effectively adjust their electronic band structure (Figure 4a).[37] Calculated from the Tauc plots, the corresponding band gap energies (E_g) of TEPY-Ni-GY, TEPY–Pd-GY, TEPY-Pt-GY and TEPY-Hg-GY were 1.16, 1.37, 1.68 and 2.18 eV, respectively (Figure S37). The reduced E_g of TEPY-Ni-GY had a positive effect on generating charge carriers during the photocatalytic process. Moreover, M–S plots performed at different frequencies (0.5 to 1.5 kHz) revealed that all samples possessed typical n-type semiconductor characteristics with positive slopes (Figures 4b and S38). The flat band potentials of TEPY-Ni-GY, TEPY-Pd-GY, TEPY-Pt-GY, and TEPY-Hg-GY were determined to be –0.96, –1.17, –1.04, and –1.21 V *vs.* Ag/AgCl (i.e., –0.76, –0.97, –0.84, and –1.01 V *vs.* NHE), respectively,

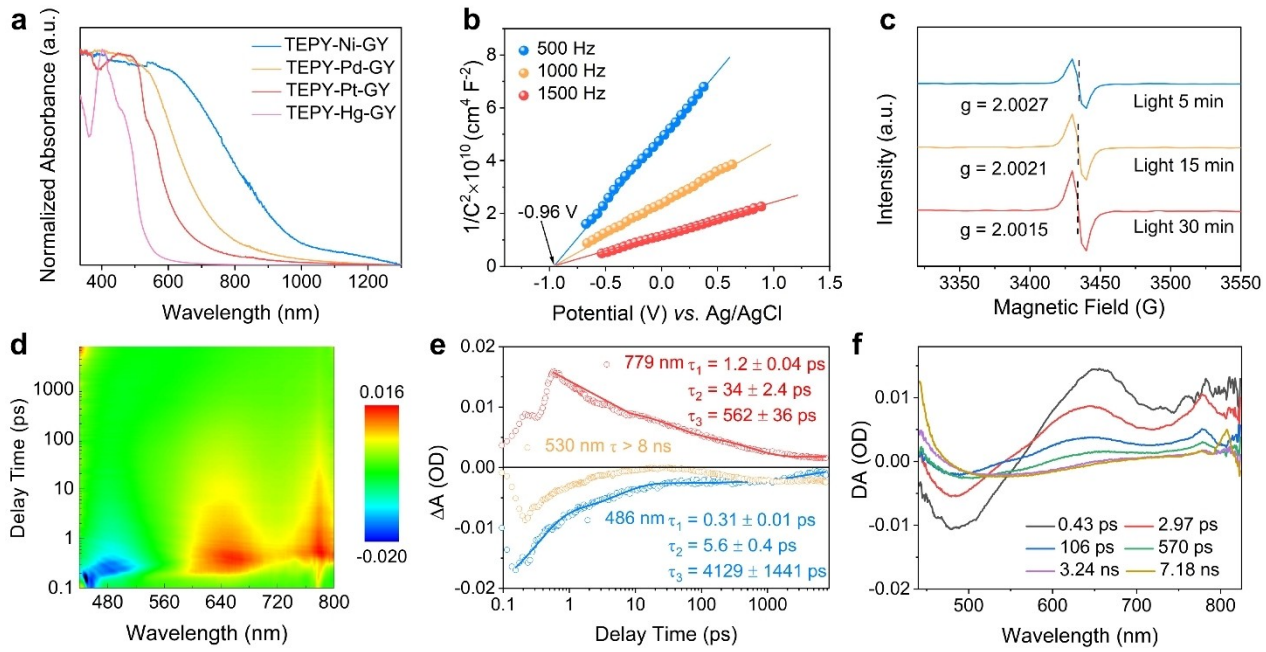

Figure 4. (a) UV-Vis DRS and (b) M–S plot for TEPY-Ni-GY. (c) EPR spectra of TEPY-Ni-GY within 30 min under visible light. (d) 2D fs-TA spectra of TEPY-Ni-GY after excitation with a 400 nm pump pulse. (e) Time slices of the transient absorption spectra for TEPY-Ni-GY excited at 400 nm. (f) fs-TA decay kinetics of TEPY-Ni-GY. The solid lines are the fittings obtained from a kinetic analysis of the transient absorption data.

which were approximately regarded as the bottom conduction band (CB) potentials. Based on the calculated band gap values and the measured CB positions, the schematic diagrams of the energy band structures of TEPY-M-GYs are depicted in Figures S39 and S40, demonstrating that all catalysts are thermodynamically feasible for the photocatalytic reduction of CO_2 to CO (CO_2/CO, theoretically at –0.53 V *vs.* NHE) under visible-light irradiation.[38–40]

Photoelectrochemical measurements were conducted to explore the electron transfer efficiency of the photocatalysts. As expected, among all samples, TEPY-Ni-GY exhibited the largest photocurrent density of 14 $\mu A\,cm^{-2}$, indicative of a greater electron accumulation due to the enhanced charge transfer. This finding was further corroborated by electrochemical impedance spectroscopy (EIS). The significantly reduced arc radius of TEPY-Ni-GY indicated a smaller charge-transfer resistance, which was more favorable for electron transport in the photocatalytic CO_2RR process.[41] (Figures S41 and S42). Furthermore, the electron paramagnetic resonance (EPR) spectra of TEPY-Ni-GY showed a Lorentzian line derived from the unpaired electrons in a highly electron-delocalized system under visible light excitation (Figure 4c). With extended illumination time, the EPR signal was enhanced, and the *g* value shifted from 2.0027 to 2.0015. In particular, a decrease in the *g*-factor is often used to illustrate an increase in spin-orbit coupling, indicating that the spin density migrated from the conjugated organic ligand to the Ni^{II} ion. This suggested that the separation and transfer of photo-generated charge carriers could be accelerated through the *d-p* orbital overlap between metal centers and adjacent alkynyl carbon.[42,43] Photoluminescence (PL) lifetime measurements also confirmed that TEPY-Ni-GY had longer excited-state lifetimes within its extended conjugated skeleton (Figure S43 and Table S4).[44]

To gain a deeper insight into the photocatalytic process, ultrafast femtosecond time-resolved transient absorption (fs-TA) measurements were performed to track the excited-state dynamics of TEPY-M-GYs in real-time. Figure 4d–f showed the fs-TA spectra for TEPY-Ni-GY following 400 nm excitation, which was dominated by a ground state bleach (GSB) signal at around 480 nm, corresponding to the band-edge transitions.[28] Over time, as the GSB signal attenuated, the band-edge bleach signal red-shifted from 480 to 530 nm, reflecting the transfer of the band-edge excited state to the metal-centered population (corresponding to the bulge at around 530 nm in the steady-state absorption spectrum, typically the absorption signal of the charge transfer transition). The kinetics at 486 nm were extracted and fitted with a tri-exponential decay function, yielding a decay lifetime of τ_3 up to about 4 ns. While the bleach at 530 nm was re-established after the initial attenuation, no further attenuation was observed. This process, with a very long lifetime of the excited state electrons, even exceeded the detection window of 8 ns, likely due to the final relaxation of the organic ligand-metal charge transfer (LMCT) state. The long-excited state lifetime was also confirmed by the non-decaying excited state absorption signal at 790 nm. The transient absorption spectrum of TEPY-Pd-GY showed a decrease in the absorption of the LMCT after excitation, with the corresponding GSB signal at around 610 nm being dominant. The kinetics of TEPY-Pd-GY probed at 600 nm were calculated by multi-exponential decays, yielding decay time constants of $\tau_1 = 0.56 \pm 0.01$ ps, $\tau_2 = 15.3 \pm 1.6$ ps, and $\tau_3 > 8$ ns. The value of τ_3 beyond the time detection window also reflects its long-excited state lifetime (Figure S44). Regarding TEPY-Pt-GY, the characteristic peaks were mainly located at approximately 70, 520, and 567 nm, consistent with the absorption of the band-to-band transition in the steady-state absorption and the transition from the ligand to the metal center. The fitted kinetics at 520 and 567 nm yielded lifetimes of about 1 and 2 ns, respectively (Figure S45). The transient spectrum of TEPY-Hg-GY was dominated by the band edges and the bleach signal corresponding to the transition of the ligand to the metal center. The fitting kinetics revealed an extremely short lifetime of only tens of ps ($\tau_1 = 0.43 \pm 0.03$ ps, $\tau_2 = 0.53 \pm 0.9$ ps, $\tau_3 = 12 \pm 1$ ps) compared with those of the other samples (Figure S46).[45–47] These results suggested that ultrafast electrons are transferred from the pyrenyl ring to the Ni^{II} catalytic center, resulting in an improved CO_2 photo-reduction efficiency. Meanwhile, these findings indicated that the type of metal ions had a significant influence on the excited-state dynamics of TEPY-M-GYs. Based on the above analysis, the appropriate introduction of metallic active sites into the GDY structure could improve the light-harvesting capabilities, expedite charge transfer kinetics, and facilitate electron accumulation at the catalytic centers for efficient CO_2 reduction.

Emission quenching experiments and fluorescence excited-state lifetimes were conducted to further elucidate the electron transfer characteristics of TEPY-Ni-GY and investigate its quenching mechanism in detail. The emission quenching experiments were performed during the photocatalytic CO_2RR without TEOA. An emission peak at 608 nm was detected with the excitation at 400 nm. As the catalyst concentration gradually increased, the fluorescence intensity significantly decreased, following a linear Stern–Volmer behavior. This indicated that the electrons generated by the excited photosensitizer $[Ru(bpy)_3]Cl_2$ could be efficiently transferred to TEPY-Ni-GY, resulting in a superior photocatalytic performance. Nevertheless, the fluorescence intensity showed almost no change when various amounts of TEOA were added to the photocatalytic system. Based on these experimental results, it could be concluded that the excited $[Ru(bpy)_3]Cl_2$ was quenched by TEPY-Ni-GY through an oxidation quenching mechanism (Figures S47–S50).[48]

In situ diffuse reflectance infrared Fourier-transform spectroscopy (DRIFTS) was performed to identify the possible intermediates generated during photocatalytic CO_2RR. The strong peaks at 2306–2381 cm^{-1} were assigned to the asymmetric stretching of CO_2 (Figure S51).[49] As displayed in Figure 5a, the characteristic peaks of various carbonate groups appeared, including absorption peaks at around 1348 and 1539 cm^{-1} assigned to monodentate carbonate (m-CO_3^{2-}), and peaks near 1306 and 1603 cm^{-1} attributed to the bidentate carbonate (b-CO_3^{2-}). Additionally, the characteristic peak at 1240 cm^{-1} was due to active

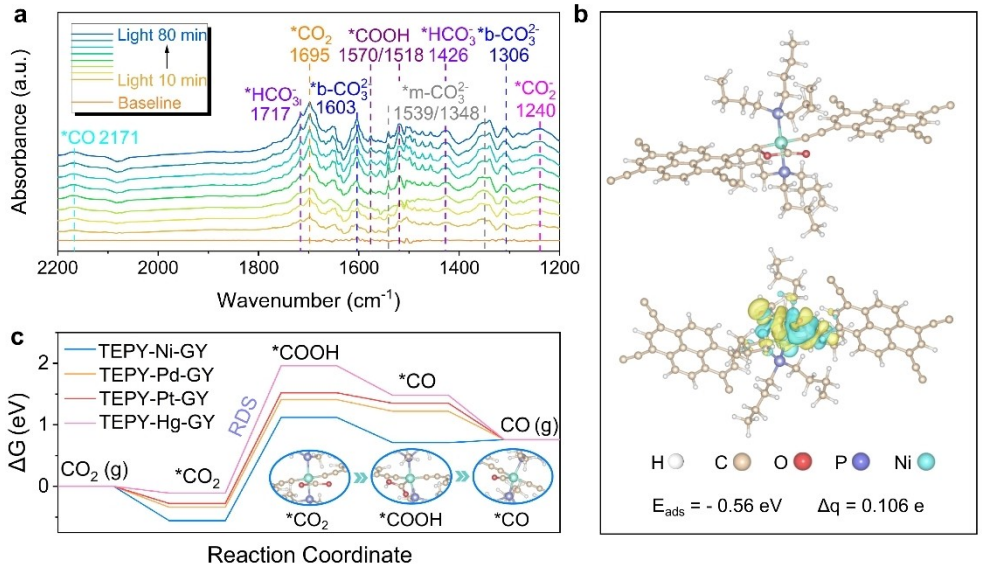

Figure 5. (a) In situ DRIFTS spectra of TEPY-Ni-GY for the simulated solar-driven CO_2 reduction process. (b) The calculated CO_2 adsorption structure. Isosurfaces (0.005) of charge density differences on the TEPY-Ni-GY with CO_2 molecules. E_{ads}: adsorption energy, △q: difference of Bader charge. Yellow and cyan iso-surfaces represent electron accumulation and electron depletion, respectively. (c) DFT-calculated Gibbs free energy (ΔG, eV) profiles for CO_2 photoreduction on TEPY-M-GYs.

$*CO_2^-$ intermediates, and the absorption peaks of bicarbonate $*HCO_3^-$ were located at 1426 and 1717 cm^{-1}.[50–52] As the primary intermediate of CO_2-to-CO conversion on the surface of TEPY-Ni-GY, *COOH originated from CO_2 hydrogenation, leading to characteristic peaks at 1518 and 1570 cm^{-1}, which was intensified with increasing irradiation time.[38] The generation of $*CO_2$ at 1695 cm^{-1} with prolonged irradiation time signified that CO_2 was activated through the reaction $CO_2 + e^- \rightarrow *CO_2$. Furthermore, a noteworthy peak at 2171 cm^{-1} indicated the formation of the *CO.[53,54] Notably, the peak intensity of the *CO intermediate greatly increased as the reaction proceeded, indicating that CO was continuously generated over time.

The CO_2 adsorption behaviors and electron distribution on the TEPY-M-GYs were investigated using density functional theory (DFT) calculations. The corresponding adsorption energies and electron transfer numbers were shown in Figures S52 and S53. The calculation results indicated that CO_2 adsorption was thermodynamically favorable on TEPY-Ni-GY, TEPY-Pd-GY, and TEPY-Pt-GY, but not on TEPY-Hg-GY, due to its weak chemical interaction with CO_2. The adsorption energy of TEPY-Ni-GY (E_{ads} = −0.56 eV) was more negative than those of TEPY-Pd-GY and TEPY-Pt-GY (Figure S54), suggesting a stronger interaction between CO_2 and TEPY-Ni-GY. As illustrated in Figure 5b, the –C≡C–Ni$(PBu_3)_2$–C≡C– moiety could adsorb CO_2 molecules through the Ni–C–O–C≡C– adsorption mode due to the synergy effect of unsaturated Ni ions (16 electrons in *d* orbital) and the π-coordination of –C≡C– blocks. Electrons are transferred to the antibonding $2\pi_u$ orbitals of CO_2, resulting in the bending of the O–C–O bond angle to 158.7° and the elongation of both C–O bonds to 1.55 Å. The C–O bond length after CO_2 adsorption on the catalyst surface was longer than the C–O bond length (1.16 Å) in a free CO_2 molecule, indicating that the bond order of the C=O bonds in the activated CO_2 was reduced.[55–56] According to the Bader method, the significant charge accumulation around the CO_2 molecule indicated a charge transfer of approximately 0.106 electron from TEPY-Ni-GY to CO_2, confirming a stronger electrostatic interaction between the CO_2 molecule and TEPY-Ni-GY.[57,58]

To gain a theoretical understanding of the superior photocatalytic CO_2RR performance of TEPY-Ni-GY and to clarify the active site characteristics of the catalysts, DFT calculations were performed using MGY frameworks as models. The Gibbs free energy diagrams for CO_2 reduction on the optimized building blocks of TEPY-M-GYs are shown in Figures 5c and S55. Generally, the photoreduction of CO_2 involves the following four steps: (i) CO_2 molecules are adsorbed on the catalyst surface to form $*CO_2$. (ii) The $*CO_2$ combines with surface protons and electrons to generate *COOH intermediate. (iii) A second proton-coupled electron transfers to *COOH and generates *CO and H_2O. (iv) The *CO desorbs from the catalysts to release CO. According to the DFT calculations, the CO_2 adsorption energy on the –C≡C–Ni$(PBu_3)_2$–C≡C– sites was calculated to be −0.56 eV, significantly lower than those for other samples, indicating that –C≡C–Ni$(PBu_3)_2$–C≡C– sites have a strong affinity for CO_2. The formation of *COOH was identified as the rate-determining step for all reactions ($*CO_2 + H^+ + e^- \rightarrow *COOH$). For TEPY-Ni-GY, the energy barrier for converting $*CO_2$ to *COOH was 1.68 eV, which was notably lower than those of the other samples (Table S5). This could be attributed to a more stable binding configuration between the –C≡C–Ni$(PBu_3)_2$–C≡C– sites and COOH* intermediates.[59] Therefore, TEPY-Ni-GY effectively stabilized the *COOH intermediates, resulting in high activity and selectivity for CO_2 reduction to CO,

consistent with the aforementioned in situ DRIFTS findings. The downhill free energy of *COOH to *CO indicated that this was a spontaneous transformation process, followed by the liberation of CO from the dissociation of the weakly bonded *CO intermediate as the final product. Moreover, the free energy of the adsorbed *H intermediate on TEPY-Ni-GY presented the highest energy barrier compared to other catalysts, demonstrating the efficient suppression of the competitive hydrogen evolution reaction following the introduction of Ni^{II} ions (Figure S56). These observations fully demonstrated that the introduction of suitable metal-bis(acetylide) moiety in the framework played a crucial role in reducing the energy barrier for CO_2 reduction and inhibiting photocatalytic hydrogen evolution, thereby enhancing the activity and selectivity of photocatalytic CO_2RR.

Based on the results from in situ DRIFTS and DFT calculations, a plausible photocatalytic mechanism for CO_2 reduction over TEPY-Ni-GY could be proposed (Figure 6). In this mechansm, the pyrenyl ring with its large π-conjugation structure acted as an electron transfer channel, expediting the separation and transfer of charge carriers. The –C≡C–Ni(PBu_3)$_2$–C≡C– sites served as the functional catalytic active centers for the adsorption and activation of CO_2. Upon visible light excitation, the $Ru(bpy)_3Cl_2$ photosensitizer was promoted to an excited state. This excited state was then oxidatively quenched by TEPY-Ni-GY, leading to the formation of $[Ru(bpy)_3]^{3+}$. During this process, electrons were transferred from the excited $[Ru(bpy)_3]^{2+}$ to the catalytic active sites. When CO_2 molecules interacted with the –C≡C–Ni(PBu_3)$_2$–C≡C– sites, electrons were transferred to the CO_2, resulting in the release of CO as a product. The residual $[Ru(bpy)_3]^{3+}$ species from the oxidative quenching pathway could be reduced back to the initial $[Ru(bpy)_3]^{2+}$ with the help of TEOA, thereby completing the photocatalytic cycle.

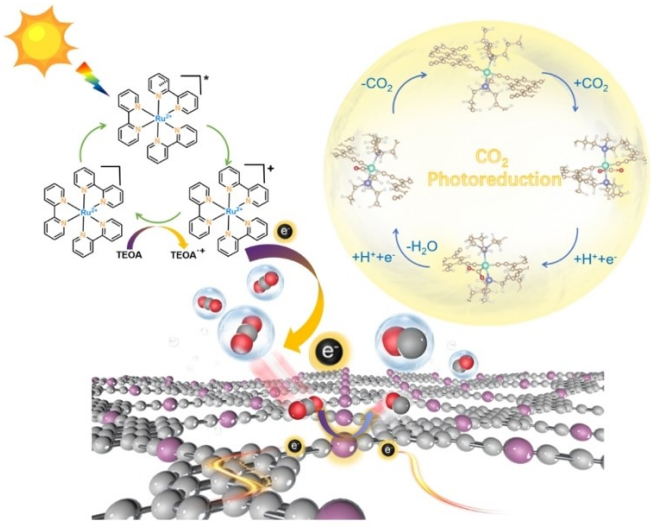

Figure 6. Proposed reaction mechanism for photocatalytic CO_2-to-CO conversion over TEPY-Ni-GY using $[Ru(bpy)_3]Cl_2$ as a photosensitizer (the two PBu_3 units in TEPY-＞Ni-GY are omitted for clarity).

Conclusions

In summary, the 2D carbon-rich frameworks of TEPY-M-GYs, combining organic frameworks and transition-metal single ions, were successfully synthesized via a base-catalyzed dehydrohalogenation reaction. These frameworks were constructed from an extended π-conjugated carbon skeleton that immobilizes transition-metal ions through diacetylene moieties. The easily accessible catalytic centers and π-conjugated structures endowed these materials with superior charge transport dynamics and catalytic performance. Additionally, the photocatalytic CO_2 reduction efficiency could be modulated by incorporating different transition-metal centers. As a result, TEPY-Ni-GY exhibited a superior CO generation rate of 18.3 mmol g^{-1} h^{-1}, selectivity of 98.8 %, and stability for 20 h under visible light irradiation. Both experimental and theoretical studies revealed that the high catalytic activity and selectivity were attributed to the synergy effects of the pyrenyl ring and Ni^{II}-bis(acetylide) moiety (–C≡C–Ni(PBu_3)$_2$–C≡C–). Therefore, this work contributes to expanding the diversity of GDY structures and illustrated that low-cost Ni^{II}-based graphyne functional materials are promising candidates in the catalytic field.

Supporting Information

The authors have cited additional references within the Supporting Information.[34–37,40,60–76]

Acknowledgements

W.-Y.W. thanks the financial support from the RGC Senior Research Fellowship Scheme (SRFS2021-5S01), the Hong Kong Research Grants Council (PolyU 15307321), Research Institute for Smart Energy (CDAQ), Research Centre for Nanoscience and Nanotechnology (CE2H), Research Centre for Carbon-Strategic Catalysis (CE2L) and Miss Clarea Au for the Endowed Professorship in Energy (847S). L.L.X. thanks the financial support from the Hong Kong Research Grants Council (PolyU 25301524), Guangdong Provincial Natural Science Foundation-General Project (2024 A1515010422), PolyU (WZ0Z, BEBA, CDB5, CE2N) and PolyU Shenzhen Research Insititute (Baichengbaiyuan special launch fund). Y.W. thanks the financial support from the National Natural Science Foundation of China (22309156).

Conflict of Interest

The authors declare no conflict of interest.

Data Availability Statement

The data that support the findings of this study are available from the corresponding author upon reasonable request.

Keywords: highly π-conjugated structure · metalated graphyne · nickel(II)-acetylide frameworks · photocatalytic CO_2 reduction

[1] G. Li, Y. Li, H. Liu, Y. Guo, Y. Li, D. Zhu, *Chem. Commun.* **2010**, *46*, 3256–3258.
[2] C. Zhang, Y. Xue, X. Zheng, L. Qi, Y. Li, *Mater. Today* **2023**, *66*, 72–83.
[3] X. Fu, X. Zhao, T. Lu, M. Yuan, M. Wang, *Angew. Chem. Int. Ed.* **2023**, *62*, e202219242.
[4] X. Zheng, Y. Xue, C. Zhang, Y. Li, *CCS Chem.* **2022**, *5*, 1653–1662.
[5] G. Hu, J. He, J. Chen, Y. Li, *J. Am. Chem. Soc.* **2023**, *145*, 5400–5409.
[6] J. Li, Y. Xue, X. Zheng, H. Wu, Y. Cao, Y. Li, *CCS Chem.* **2024**, *0*, 1–8.
[7] J. Yu, W. Chen, F. He, W. Song, C. Cao, *J. Am. Chem. Soc.* **2023**, *145*, 1803–1810.
[8] C. Zhang, X. Zheng, Y. Gao, C. Xing, S. Chen, Y. Xue, Y. Li, *Natl. Sci. Rev.* **2024**, *11*, nwae189.
[9] Y. Fang, Y. Liu, L. Qi, Y. Xue, Y. Li, *Chem. Soc. Rev.* **2022**, *51*, 2681–2709.
[10] L. Qi, Y. Gao, Y. Gao, Z. Zheng, X. Luan, S. Zhao, Z. Chen, H. Liu, Y. Xue, Y. Li, *J. Am. Chem. Soc.* **2024**, *146*, 5669–5677.
[11] Y. Gao, Z. Cai, X. Wu, Z. Lv, P. Wu, C. Cai, *ACS Catal.* **2018**, *8*, 10364–10374.
[12] Y. Xue, B. Huang, Y. Yi, Y. Guo, Z. Zuo, Y. Li, Z. Jia, H. Liu, *Nat. Commun.* **2018**, *9*, 1460.
[13] J. Liu, L. Zhang, K. Wang, C. Jiang, C. Zhang, N. Wang, *Adv. Funct. Mater.* **2023**, *49*, 2305254.
[14] G. Shi, Y. Xie, L. Du, X. Fu, X. Chen, W. Xie, T. Lu, M. Yuan, M. Wang, *Angew. Chem. Int. Ed.* **2022**, *134*, e202203569.
[15] X. Yin, S. Tang, C. Zhang, H. Wang, R. Si, X. Lu, T. Lu, *J. Mater. Chem. A* **2020**, *8*, 20925–20930.
[16] X. Yin, H. Wang, S. Tang, X. Lu, M. Shu, R. Si, T. Lu, *Angew. Chem. Int. Ed.* **2018**, *57*, 9382–9386.
[17] H. Liu, D. Yan, X. Zhang, H. Wu, J. Li, Y. Li, *Angew. Chem. Int. Ed.* **2023**, *62*, e202216739.
[18] H. Zou, W. Rong, S. Wei, Y. Ji, L. Duan, *PNAS* **2020**, *117*, 29462–29468.
[19] X. Fu, X. Zhao, T. Lu, M. Yuan, M. Wang, *Angew. Chem. Int. Ed.* **2023**, *62*, e202219242.
[20] Z. Yang, J. L. Gebhardt, T. A. Schaub, T. Sander, J. Schönamsgruber, H. Soni, A. Görling, M. Kivala, S. Maier, *Nanoscale* **2018**, *10*, 3769–3776.
[21] Q. Sun, L. Cai, H. Ma, C. Yuan, W. Xu, *ACS Nano* **2016**, *10*, 7023–7030.
[22] L. Xu, J. Sun, T. Tang, H. Zhang, M. Sun, J. Zhang, J. Li, B. Huang, Z. Wang, Z. Xie, W.-Y. Wong, *Angew. Chem. Int. Ed.* **2021**, *60*, 11326–11334.
[23] M. Fang, L. Xu, H. Zhang, Y. Zhu, W.-Y. Wong, *J. Am. Chem. Soc.* **2022**, *144*, 15143–15154.
[24] Y. Zhao, L. Xu, X. Wang, Z. Wang, Y. Liu, Y. Wang, Q. Wang, Z. Wang, H. Huang, Y. Liu, W.-Y. Wong, *Nano Today* **2022**, *43*, 101428.
[25] Y. Yamazaki, M. Miyaji, O. Ishitani, *J. Am. Chem. Soc.* **2022**, *144*, 6640–6660.
[26] Y. Cao, L. Guo, M. Dan, D. E. Doronkin, C. Han, Z. Rao, Y. Liu, J. Meng, Z. Huang, K. Zheng, P. Chen, F. Dong, Y. Zhou, *Nat. Commun.* **2021**, *12*, 1675.
[27] S. Wang, X. Hai, X. Ding, S. Jin, Y. Xiang, P. Wang, B. Jiang, F. Ichihara, M. Oshikiri, X. Meng, Y. Li, W. Matsuda, J. Ma, S. Seki, X. Wang, H. Huang, Y. Wada, H. Chen, J. Ye, *Nat. Commun.* **2020**, *11*, 1149.
[28] Z. Fang, T. Liu, J. Liu, S. Jin, X. Wu, X. Gong, K. Wang, Q. Yin, T. Liu, R. Cao, H. Zhou, *J. Am. Chem. Soc.* **2020**, *142*, 12515–12523.
[29] W. Chen, L. Wang, D. Mo, F. He, Z. Wen, X. Wu, H. Xu, L. Chen, *Angew. Chem. Int. Ed.* **2020**, *59*, 16902–16909.
[30] J. He, N. Wang, Z. Cui, H. Du, L. Fu, C. Huang, Z. Yang, X. Shen, Y. Yi, Z. Tu, Y. Li, *Nat. Commun.* **2017**, *8*, 1172.
[31] M. Dong, J. Zhou, J. Zhong, H. Li, C. Sun, Y. Han, J. Kou, Z. Kang, X. Wang, Z. Su, *Adv. Funct. Mater.* **2022**, *32*, 2110136.
[32] J. Li, X. Gao, X. Jiang, X. Li, Z. Liu, J. Zhang, C.-H. Tung, L. Wu, *ACS Catal.* **2017**, *7*, 5209–5213.
[33] H. Zhang, Z. Lin, P. Kidkhunthod, J. Guo, *Angew. Chem. Int. Ed.* **2023**, *135*, e202217527.
[34] L. Wang, Z. Han, Q. Zhao, X. Yao, Y. Zhu, X. Ma, S. Wu, C. Cao, *J. Mater. Chem. A* **2020**, *8*, 8612–8619.
[35] H. Zheng, J. Zhao, Y. Sun, A. Zhang, Y. Cheng, L. He, X. Bu, J. Zhang, Q. Lin, *J. Am. Chem. Soc.* **2023**, *145*, 27728–27739.
[36] W. Zhong, R. Sa, L. Li, Y. He, L. Li, J. Bi, Z. Zhuang, Y. Yu, Z. Zou, *J. Am. Chem. Soc.* **2019**, *141*, 7615–7621.
[37] S. Yang, R. Sa, H. Zhong, H. Lv, D. Yuan, R. Wang, *Adv. Funct. Mater.* **2022**, *32*, 2110694.
[38] Q. Zhang, S. Gao, Y. Guo, H. Wang, J. Wei, X. Su, H. Zhang, Z. Liu, J. Wang, *Nat. Commun.* **2023**, *14*, 1147.
[39] Y. Li, S. Wang, X. Wang, Y. He, Q. Wang, Y. Li, M. Li, G. Yang, J. Yi, H. Lin, D. Huang, L. Li, H. Chen, J. Ye, *J. Am. Chem. Soc.* **2020**, *142*, 19259–19267.
[40] X. Dong, Y. Si, Q. Wang, S. Wang, S. Zang, *Adv. Mater.* **2021**, *33*, 2101568.
[41] Y. Qin, H. Li, J. Lu, Y. Feng, F. Meng, C. Ma, Y. Yan, M. Meng, *Appl. Catal. B-Environ.* **2020**, *277*, 119254.
[42] Y. Kutin, N. Cox, W. Lubitz, A. Schnegg, O. Rüdiger, *Catalysts* **2019**, *9*, 926.
[43] X. Zhang, G. Lu, *Carbon* **2016**, *108*, 215–224.
[44] Y. Qin, H. Li, J. Lu, F. Meng, C. Ma, Y. Yan, M. Meng, *Chem. Eng. J.* **2020**, *384*, 123275.
[45] X. Fang, Q. Shang, Y. Wang, L. Jiao, T. Yao, Y. Li, Q. Zhang, Y. Luo, H. Jiang, *Adv. Mater.* **2018**, *30*, 1705112.
[46] L. Ran, Z. Li, B. Ran, Y. Zhao, T. Shao, Y. Song, M. K. H. Leung, L. Sun, J. Hou, *J. Am. Chem. Soc.* **2022**, *144*, 17097–17109.
[47] S. Chen, K. Li, F. Zhao, L. Zhang, M. Pan, Y. Fan, J. Guo, J. Shi, C. Su, *Nat. Commun.* **2016**, *7*, 13169.
[48] J. Wang, L. Qian, H. Nie, H. Huang, Y. Li, S. Yao, M. Liu, Z. Zhang, Z. Kuang, T. Lu, *Nat. Commun.* **2021**, *12*, 813.
[49] S. Guo, Y. Xiao, B. Jiang, *ACS Sustain. Chem. Eng.* **2021**, *9*, 12646–12654.
[50] J. Zhou, J. Li, L. Kan, L. Zhang, Q. Huang, Y. Yan, Y. Chen, J. Liu, Y. Lan, *Nat. Commun.* **2022**, *13*, 4681.
[51] L. Cheng, X. Yue, L. Wang, D. Zhang, P. Zhang, J. Fan, Q. Xiang, *Adv. Mater.* **2021**, *33*, 2105135.
[52] P. Deng, M. Gan, X. Zhang, Z. Li, Y. Hou, *Int. J. Hydrogen Energy* **2019**, *44*, 30084–30092.
[53] K. Sun, Y. Qian, H. Jiang, *Angew. Chem. Int. Ed.* **2023**, *62*, e202217565.
[54] X. Li, Y. Sun, J. Xu, Y. Shao, J. Wu, X. Xu, Y. Pan, H. Ju, J. Zhu, Y. Xie, *Nat. Energy* **2019**, *4*, 690–699.
[55] Y. Chai, Y. Kong, M. Lin, W. Lin, J. Shen, J. Long, R. Yuan, W. Dai, X. Wang, Z. Zhang, *Nat. Commun.* **2023**, *14*, 6168.
[56] X. Ye, C. Yang, X. Pan, J. Ma, Y. Zhang, Y. Ren, X. Liu, L. Li, Y. Huang, *J. Am. Chem. Soc.* **2020**, *142*, 19001–19005.
[57] Z. Yan, M. Du, J. Liu, S. Jin, C. Wang, G. Zhuang, X. Kong, L. Long, L. Zheng, *Nat. Commun.* **2018**, *9*, 3353.

[58] W. Lyu, Y. Liu, J. Zhou, D. Chen, X. Zhao, R. Fang, F. Wang, Y. Li, *Angew. Chem. Int. Ed.* **2023**, *62*, e202310733.
[59] H. Zheng, S. Huang, M. Luo, Q. Wei, E. Chen, L. He, Q. Lin, *Angew. Chem. Int. Ed.* **2020**, *59*, 23588–23592.
[60] H. Maciejewski, B. Marciniec, J. Gulinski, A. Karolak, N. K. Skvortsov, *Inorg. Chem. Commun.* **2002**, *5*, 464–467.
[61] M. Yang, L. Zhang, Z. Lei, P. Ye, J. Si, Q. Yang, Y. Wang, *J. Appl. Polym. Sci.* **1998**, *70*, 1165–1172.
[62] G. Kresse, J. Furthmüller, *Comp. Mater. Sci.* **1996**, *6*, 15–50.
[63] G. Kresse, D. Joubert, *Phys. Rev. B* **1999**, *59*, 1758–1775.
[64] P. E. Blöchl, *Phys. Rev. B* **1994**, *50*, 17953–17979.
[65] J. P. Perdew, K. Burke, *Phys. Rev. Lett.* **1996**, *77*, 3865–3868.
[66] M. Methfessel, A. T. Paxton, *Phys. Rev. B* **1989**, *40*, 3616–3621.
[67] J. D. Pack, H. J. Monkhorst, *Phys. Rev. B* **1977**, *16*, 1748–1749.
[68] S. Grimme, *J. Comput. Chem.* **2006**, *27*, 1787–1799.
[69] V. Wang, N. Xu, J. Liu, G. Tang, W. Geng, *Comput. Phys. Commun.* **2021**, *267*, 108033.
[70] M. Dong, J. Zhou, J. Zhong, H. Li, C. Sun, Y. Han, J. Kou, Z. Kang, X. Wang, Z. Su, *Adv. Funct. Mater.* **2022**, *32*, 2110136.
[71] H. Zhong, R. Sa, H. Lv, S. Yang, D. Yuan, X. Wang, R. Wang, *Adv. Funct. Mater.* **2020**, *30*, 2002654.
[72] H. Zheng, S. Huang, M. Luo, Q. Wei, E. Chen, L. He, Q. Liu, *Angew. Chem. Int. Ed.* **2020**, *132*, 23794–23798.
[73] B. Han, X. Ou, Z. Deng, Y. Song, C. Tian, H. Deng, Y. Xu, Z. Lin, *Angew. Chem. Int. Ed.* **2018**, *57*, 16811–16815.
[74] W. Yang, H. Wang, R. Liu, J. Wang, C. Zhang, C. Li, D. Zhong, T. Lu, *Angew. Chem. Int. Ed.* **2021**, *60*, 409–414.
[75] J. Wang, W. Zhu, F. Meng, G. Bai, Q. Zhang, X. Lan, *ACS Catal.* **2023**, *13*, 4316–4329.
[76] X. Wang, J. Liu, L. Zhang, L. Dong, S. Li, Y. Kan, D. Li, Y. Lan, *ACS Catal.* **2019**, *9*, 1726–1732.

Manuscript received: September 23, 2024
Accepted manuscript online: October 4, 2024
Version of record online: November 7, 2024